Structural imperfections in additive manufacturing perceived from the X-ray micro-tomography perspective

Hedi Nouri, Sofiane Guessasma, Sofiane Belhabib

Journal of Materials Processing Technology 234 (2016) 113–124

Contents lists available at ScienceDirect

Journal of Materials Processing Technology

journal homepage: www.elsevier.com/locate/jmatprotec

Structural imperfections in additive manufacturing perceived from the X-ray micro-tomography perspective

Hedi Nouri [a,b], Sofiane Guessasma [c,*], Sofiane Belhabib [d]

[a] Mines Douai, Department of Polymers and Composites Technology & Mechanical Engineering (TPCIM), 941 Rue Charles Bourseul, CS 10838, 59508 Douai, France
[b] Ecole Nationale d'Ingénieurs de Sfax, Laboratoires des Systèmes Electromécaniques, Route Soukra Km 3, BPW 3038 Sfax, Tunisia
[c] INRA, UR1268 Biopolymères Interactions Assemblages, F-44300 Nantes, France
[d] LUNAM Université Nantes Angers Le Mans, CNRS, GEPEA, UMR 6144, IUT de Nantes, 2 Avenue du Professeur Jean Rouxel, 44475 Carquefou Cédex, France

ARTICLE INFO

Article history:
Received 13 November 2015
Received in revised form 17 March 2016
Accepted 20 March 2016
Available online 22 March 2016

Keywords:
Additive manufacturing
Acrylonitrile Butadiene Styrene
X-ray micro-tomography
Fused deposition modelling
Structural anisotropy

ABSTRACT

Our concern is to reveal the extent of structural imperfections of Additive Manufacturing (AM) by considering 3D imaging technique based on X-ray micro-tomography. Blocks of Acrylonitrile Butadiene Styrene (ABS) polymer are processed using Fused Deposition Modelling (FDM) with different printing orientations. Image analysis is applied to the stacks of 3D printed blocks to quantify structural attributes such as porosity content and connectivity.

The results show that pore connectivity represents the most important structural characteristic of FDM. The adopted commercial solution is able to produce acceptable porosity contents below 6% regardless of the printing orientation. Finite element results indicate the presence of expected transverse symmetry. The examination of the extent of such anisotropy is in well agreement with the observed structural imperfections mainly the porosity content. However, these predictions do not match the wide variations in mechanical performance described in the literature. The finite element analysis guides the next research step towards quantification of the imperfect bonding nature between filaments in FDM.

1. Introduction

Additive Manufacturing (AM) is presented by (Zhai et al., 2014) as the second industrial revolution of this epoch. The authors show that this term is justified by the wide impact triggered by such technology on modern society, allowing mostly anyone to be a designer.

AM is now attracting animated debates in different disciplines of research. Huang et al. (2013) point out two major concerns that need further investigation: energy and health footprints. For instance, various healthcare products can be personalised using additive manufacturing such as implants, safety equipment and other products related to tissue engineering. The same authors (Huang et al., 2013) show the positive impact of AM on energy demand with two main driving factors, namely reduction and efficiency. This impact is justified by the ability to design products of a lower energy consumption using limited amount of materials and fluids. All these aspects are expected to improve the environmental impact and product life time. Kietzmann et al. (2015) show that some of these debates are related to ethical and legal issues driven by the new role of consumer in the market. This is illustrated by the opposition between company innovation effort and consumer creativity for the design products that have certain conformity. Versatile techniques of additive manufacturing are able to shorten fabrication steps to one main between the CAD design and the real part. As shown in the review work of Pham and Gault (1998), the reduced number of manufacturing steps, for a large number of AM processes, is a vector for enhancing the competitiveness and an open gateway for optimising manufacturing cost. This comes with a certain cost as detailed in the survey by Yan and Gu (1996), which points out the limited performance, lack of accuracy and short window for material selection. All these aspects are now a major research area in AM. For instance, recent advances in electron beam melting show a large potential to control the porous structure in 3D printed cellular materials (Li et al., 2016). Such fine control of the microstructure allows the development of functionally graded materials that present advantageous biological functions such as osteoblast in bioengineering applications (Nune et al., 2016a,b, 2014).

* Corresponding author.
E-mail address: sofiane.guessasma@nantes.inra.fr (S. Guessasma).

http://dx.doi.org/10.1016/j.jmatprotec.2016.03.019
0924-0136/

Research literature on the subject agrees that the primary characteristic of additive manufacturing is the ability to design complex geometries. Becker et al. (2005) show that this is a real opportunity to rethink the design without being bounded by the tooling constrain. Fused deposition modelling FDM is one the popular way of additive manufacturing. The early review on the subject by Pham and Gault (1998) categorises FDM as liquid-based additive manufacturing. Turner et al. (2014) describe FDM as a typical extrusion process, where the filament of the feed material is swiped from the support cartridge using driving wheels. The material is forced to the liquid state using a liquefier and the fused material flows from the printing tip to the modelling base. This tip is able to move relatively to the printing base in the three dimensional space. Most of the printed materials using FDM are polymers (mainly Acrylonitrile Butadiene Styrene or ABS, Polylactic acid or PLA). Recently, Carneiro et al. (2015) demonstrate the feasibility of using polypropylene as a polymer candidate in FDM starting from the filament extrusion step and ending to the small size part characterisation.

The result of lying down of the fused matter in successive layers is the development of anisotropic structuring. Ahn et al. (2002) show a strong correlation between the raster angle and the tensile properties of ABS. The authors show that tensile strength can vary in a wide range (from 2.5 to 20 MPa) depending on inter-filament crossing and orientation. Lee et al. (2007) show that failure modes under compression are distinct depending on the choice of AM technology. Shaffer et al. (2014) show that improved macromolecular crosslinking in FDM-based thermoplastic systems is achievable using gamma radiation. The authors highlight a direct consequence on increased toughness of studied polymers. These contributors (Shaffer et al., 2014) confirm that tensile responses of PLA and ABS samples are sensitive to printing orientation. The optimal response corresponds to the maximum alignment of filament in the loading direction. In addition, the results of the same authors indicate higher sensitivity of ABS compared to PLA to mechanical anisotropy. The literature work is constantly exhibiting attempts to reduce anisotropy issues by, for example, optimising the part orientation or applying post-processing to improve cross-linking. Carneiro et al. (2015) show that, besides the part orientation prevailing effect, the infill degree has also a strong effect on tensile properties of PP and PP based composites. Thrimurthulu et al. (2004) suggest the use of optimisation strategy based on genetic algorithm to achieve optimal deposition orientation with reduced stair-case effect and minimum support material. Strategies also are applied to reduce discontinuities by considering more continuous modes of printing. Chakraborty et al. (2008) argue on the benefits of using curved layer FDM to improve the processing of curved structures such as thin shell-type parts. The authors show that the reduction of the stair-case effect and smooth finishing surface state are important outcomes of the proposed FDM strategy. Choi et al. (2011) present a modified commercial set-up with capabilities of vertical layering. The authors claim that this modified set-up allows more flexibility by reducing the dependence to the building direction. For a large number of these contributions, the optimal design in AM is conducted from an engineering viewpoint, by focusing on process parameter driven effects. For instance, Galantucci et al. (2008) focus on optimising manufacturing time and cost with respect to shape factors such as the internal angle, raster and shell width. In a review paper, Mohamed et al. (2015) show that the FDM optimisation relies on building orientation, layer thickness and tool path parameters. The authors refer to the literature work to relate these influential parameters to surface roughness, part deposition imprecision, building time, and part performance.

Better actions towards the optimal design can be driven by more fundamental understanding of the nature and extent of the defects induced by AM. Thanks to the recent advances in 3D image techniques, it is now possible to achieve a clear picture of the texture and defect extent at the microstructure scale (Baker et al., 2012; Maire and Withers, 2014; Mizutani and Suzuki, 2012). This is illustrated in the work of Mostefai et al. (2015), which suggests the use of X-ray micro-tomography to achieve microstructural arrangement in heterogeneous cementiteous composite. This picture can be even more accurate if an anticipation of the microstructural performance is included through computational analysis (Moreno-Atanasio et al., 2010). This is conducted in the work of Ayadi et al. (2015), where the authors are able to combine finite element analysis and X-ray micro-tomography imaging to predict the elasticity behaviour of polymeric composites. These two types of analysis, namely X-ray micro-tomography and finite element computation are brought together in this research contribution to gain more fundamental knowledge about the process-induced defects.

Indeed, X-ray micro-tomography is used, in this study, to quantify the defects in the three-dimensional space. Part of the analysis is the determination of the porous structure and related attributes. The 3D images are converted into finite element model to capture the effect of process-induced defects on the mechanical performance of the printed parts. This study focuses on ABS polymer blocks that are printed using a commercial FDM solution.

2. Experimental layout

The ABS polymer is delivered by CADvision company (Guyancourt, France) under the reference P430XL ABS. The additive manufacturing is based on commercial solution of fused deposition modelling manufacturing. Processing is performed using uPrint SE 3D printer from Stratasys. This printing technology is equipped with two tips of 254 μm in diameter each for the deposition of ABS and a dissolvable support. Cuboids of ABS ($30 \times 30 \times 30$) mm^3 are printed using different orientations with respect to the modelling base. Orientation is represented by the angle θ, where the following choices are made 0°, 30°, 45°, 60°, and 90° (Fig. 1). The Stl files of the CAD models are transformed into tool paths using built-in software (CatalystEX). Due to the simplicity of the CAD model, the software plans soluble support at the first layers to prevent strong bonding to the base.

X-ray micro-tomography characterisation of the printed samples is conducted using an UltraTom X-ray μ-CT system. The acquisition parameters are: voltage 60 KV, current intensity 480 μA, voxel size 30 μm, continuous mode acquisition, resolution of 2D radiographic Images 1920×3536 pixels with varian detector focused on a scintillating material, 1440 radiographic images.

We need to mention that the accuracy of 3D imaging acquisition relies on the voxel size which is eight times smaller than the printing tip diameter. Stacks representing the acquired volumes are built from the collection of radiographic images using the filtered back-projection algorithm (X-Act software from Rx-Solutions). The image acquisition and the stack assembling require less than 30 min per condition. The voxel number per stack varies is of the order of one billion.

The clear separation between the solid and air phases allows the successful application of varieties of image operators, which are coded using the programming environment of ImageJ (http://imagej.nih.gov/ij/, National Institute of Health) software from the public domain. In particular, automatic thresholding is applied to grey level stacks to achieve binary images representing air and dense phases. Flooding is applied to separate the background from the air phase. Flooding is based on the flood filling tool available in ImageJ. Since the contour of the acquired ABS block is closed, we did not use sophisticated contour detection algorithms such like wrapping developed in (Mamlouk and Guessasma, 2013) to separate accurately the background from the feature of interest. Flooding is realised on binary images starting from a background pixel. All

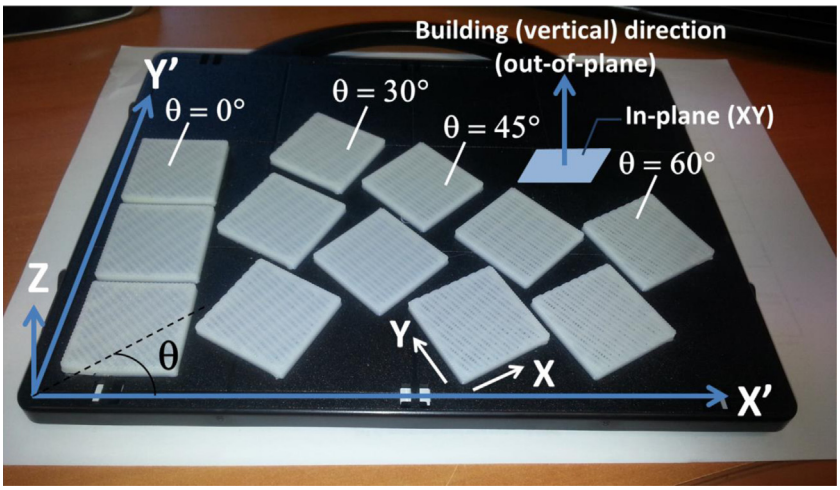

Fig. 1. Illustration of the part orientation and definition of the printing angle θ.

neighbouring pixels which have the same grey level are attributed an intermediate grey level of 128. The process is extended to all slices of the image. As a result, the background appears distinct from the porous and solid phases. Note that this operation is possible because printing of ABS is realised using a filled contour.

Pore size distribution is obtained using granulometry technique (Guessasma et al., 2008). The size distribution determination is based on a growing structural element that scans the stack with a regular step. Each time a feature of size less than the size of the structuring element is detected, it is eliminated from the foreground. This corresponding size frequency is incremented accordingly. The computation time may be significant to assess the pore size distribution. Indeed, a large number of scanning steps is needed to scan the stack. This process is repeated for each size increment (one voxel) of the structuring element, which requires additional saving of intermediate stacks. The last iteration corresponds to the largest detected feature in the foreground. This algorithm works thus as a numerical sieving technique. Granulometry technique is efficient to measure the pore polydispersity but it hardly estimates pore connectivity. This last feature is captured from 3D labelling technique. Since pores are viewed as collection of voxels, they are connected if they share common faces, edges or corners. Pore connectivity can be assessed from analysis of porosity volume distribution. 3D labelling technique allows the determination of the largest connected feature using face, edge or corner connectivity defined by the operator. If two voxels belonging to two globular porosities (or identified as distinct features from granulometry analysis) share a face or an edge, these are considered as part of the same feature. A measure of pore connectivity would be to scale the largest connected feature with respect to the sum of all labelled features. The ratio (largest feature volume/total pore network volume) is large for a highly connected pore network. One may notice that this ratio is a bounded quantity (between 0 and 1), which makes it easier to rank pore connectivity of printed ABS blocks as function of printing angle θ.

Labelling is performed using 26 connectivity scheme in which voxels belong to the same feature if they share face or corner in common. With this last process, information about pore connectivity can be gained by scaling the largest pore volume with respect to the total volume of available porosity. It is common to find in the literature percolation analysis based on lower connectivity scheme such as face connectivity. From the perspective of relating pore connectivity results to elasticity constants; such scheme will be too restrictive. Indeed, if two pores are connected through an edge, opening and thus localisation occurs even if loading is limited. The use of face connectivity reduces the connectivity to the first neighbours and obviously affects the magnitude of pore percolation. This effect is further investigated. Granulometry and 3D labelling are time consuming technique especially for large stacks. The size distribution determination of the porous network is the most resource consuming technique even if the developed algorithm is optimised in terms of memory and CPU (Central Processing Unit) management. Indeed, the duration of processing varies from 2 days to 5 days per stack on workstation equipped with 24-core Xeon CPU E5-2620 and 192 GB of RAM.

Several structural attributes are measured from the processed images. The porosity content is determined using the expression

$$f(\%) = 100 \times \left(\sum_{i=1}^{n \times m \times l} \delta_i^1 (g_i) / \sum_{i=1}^{n \times m \times l} \delta_j^2 (g_j) \right) \quad (1)$$

where

$$\delta_i^1 (0) = 1; \delta_i^1 (128) = 0; \delta_i^1 (255) = 0 \quad (2)$$

and

$$\delta_j^2 (0) = 1; \delta_j^2 (128) = 0; \delta_j^2 (255) = 1 \quad (3)$$

and $f(\%)$ is the porosity volume percentage, δ_i is the Kronecker function, which depends on the grey level g_i associated to voxel i; n, m and l are the dimensions of the X-ray image in X, Y and Z directions, respectively. Z-axis is the building-up direction associated to the 3D printed ABS samples.

In addition to the overall porosity content $f(\%)$, the axial contributions are accounted to measure the anisotropy inferred to the process. The average porosity content per cross-section area is plotted against the slice number. For example, the porosity content in the direction of sample growth $f_z(i)$ at a particular slice number i reads

$$f_z(i) = 100 \times \left(\sum_{j=(i-1)\times n \times m+1}^{(i)\times n \times m} \delta_j^1 (g_j) / \sum_{k=(i-1)\times n \times m}^{(i)\times n \times m} \delta_k^2 (g_k) \right) \quad (4)$$

The scatter of the porosity content in the same direction δf_z is calculated using the definition of the standard deviation

$$\delta f_z(\%) = \sqrt{(1/l) \times \sum_{i=1}^{l} \left(f_z(i) - \left(\sum_{i=1}^{l} f_z(i)/l \right) \right)^2} \quad (5)$$

Similar expressions are derived for $\delta f_x(\%)$ and $\delta f_y(\%)$.

The largest porosity level *Mxf* is also measured in all space directions from the statistics on all available cross-sections. In Z-direction, this implies

$$Mxf_z = Max_{i=1}^{l}\left(f_z(i)\right) \tag{6}$$

where Mxf_z is the peak porosity level measured in Z-direction. Equivalent expressions can be derived for Mxf_x and Mxf_y.

Pore connectivity is measured using

$$\gamma(\%) = 100 \times Max_{i=1}^{N}\left(V_p(i)\right) / \sum_{i=1}^{N} V_p(i) \tag{7}$$

where γ is the pore connectivity percentage, $V_p(i)$ is the volume associated to the labelled pore i, N is the total pore number.

We perform both 26-connectivity (γ_{26}) and 6-connectivity (γ_6) analysis to compare the loss of pore connectivity when only first nearest voxel neighbours are used.

3. Modelling technique

The purpose of the Finite element analysis is to quantify the effect of microstructural imperfections by looking at the stress and strain fields for different printing orientations. Ansys multi-physics commercial package (ANSYS Inc., Canonsburg, PA, USA) is used for all finite element computations. The acquired stacks are imported as regular meshes using voxel to element conversion (Ayadi et al., 2015). The model size is proportional to the image resolution. It is adapted to allow computations to be performed under hundreds of millions of degrees of freedom. The limited computation resources (time and memory requirement) impose the lowering of the image resolution by a factor λ^3 such that

$$\lambda^3 = N_\lambda / N_0 \tag{8}$$

where N_0 and N are the total number of voxels in the original and new images.

The resolution coarsening can be further defined using dimensions *n, m* and *l* of the X-ray original images

$$N_\lambda = \left(n/\lambda\right) \times \left(m/\lambda\right) \times \left(l/\lambda\right) \tag{9}$$

Finite element computations are conducted using a coarsening factor of 0.25 ($\lambda^3 = 1/64$).

All finite element computations are conducted exclusively using the above mentioned coarsening factor. However, structural attributes such as phase content and pore connectivity are determined for a large interval of coarsening factors ($\lambda \geq 0.025$) up to the original resolution ($\lambda = 1$). Change of the phase content and pore connectivity may occur as a result of the resolution degradation. The accuracy of the voxel to element conversion is checked by monitoring phase content and pore connectivity variation for a decreasing resolution.

Meshing relies on structural elements defined by 8 nodes and three structural displacements per node in X, Y and Z directions. The element size of 120 μm is still smaller than the tip diameter of the 3D printer. Computations are performed based on a full stack for all orientations but also on substacks representing fractions from the full volume. Cropping is realised in both lateral (X,Y) and building (Z) directions. The new z-dimension in normal sampling using

$$z = \alpha \times Z | \alpha = 0.1, \ldots, 1.0 \tag{10}$$

Ten levels are used, and these corrrespond to 30 finite element evaluations per orientation. In these computations, remaining dimensions X and Y of each domain are kept at the full scale.

For lateral sampling, a similar expression is used

$$\begin{cases} x = \beta \times X | \beta = 0.1, \ldots, 1.0 \\ y = \beta \times Y | \beta = 0.1, \ldots, 1.0 \end{cases} \tag{11}$$

The same number of levels is used and the Z dimension is kept at full scale.

The model size varies depending on sampling from few thousands to few dozens of millions of dof (i.e., degrees of freedom).

Isotropic elastic material model is implemented for the dense ABS phase (E_S = 1.54 GPa, ν_S = 0.35, where E_S is Young's modulus and ν_S is Poisson's coefficient).

Periodic boundary conditions are used to predict stress and strain distributions in the printed blocks in three loading directions X, Y and Z.

Regular meshing allows using homologue nodes to apply periodic boundary conditions. Homologue nodes are identified for opposed faces as

$$R_{i_1 j_1 k_1} = R_{i_2 j_2 k_2} + D | D = D_x, D_y, D_z \tag{12}$$

where R and D are vectors, the magnitude and orientation of D are associated to one of the physical dimensions of the acquired volume, $i_1, j_1, k_1, i_2, j_2, k_2$ are indices related to voxel locations R in the image.

Constraints equations can be expressed using

$$U_{i_1 j_1 k_1} = U_{i_2 j_2 k_2} + \Delta U \tag{13}$$

where U represents nodal displacement vector, U is a constant vector, nodes satisfying the constraint equations are determined using equation (12).

Since boundary conditions are applied as constrain equations (coupling equations), the strain and displacement fields are not known in advance at lateral faces. When solving the elasticity problem, these quantities become available for all nodes including those belonging to the lateral faces. The average of lateral displacements for all nodes belonging to the external surfaces (those associated to the cropped volume) is used to compute Poisson's ratios at any sampling ratio.

In addition, Young's moduli are derived from nodal reaction forces knowing the imposed displacement whereas Poisson's ratios are determined from the average displacement of lateral faces. Three Young's moduli (EX, EY and EZ) and six Poisson's ratios (ν_{yx}, ν_{zx}, ν_{xy}, ν_{zy}, ν_{xz}, and ν_{yz}. where ν_{ij} refers to the lateral expansion in i-direction for an imposed compression in j-direction) are computed for each run. The computation duration per loading point reaches 2 h performed on 24-core Xeon CPU E5-2620 workstation equipped with 192 GB of RAM.

4. Results and discussion

Fig. 2 shows qualitatively the type of defects identified from X-ray micro-tomography analysis. On the top right side, typical pore morphology is shown. Dimensions of the order of hundreds of microns and even millimetric scale porosities are identified. These are characterised by large arms representing the connectivity shared with other globular porosities. On the bottom right side, topography of external surfaces is exposed. Both average and maximum roughness are also given.

The central views are inner and outer perspectives of the ABS block. The left side shows close views of the filament arrangements. Two distinct dimensions are highlighted for the filament arrangement in Fig. 2: out-of-plane (Z-axis) is the building direction associated to the vertical sampling. The in-plane dimension (XY plane) is related to the laying down plane, which is represented in many studies by the raster angle or, in this study, referred by the printing angle θ.

Despite removal efforts, some residual support material still adheres to the 3D ABS structure. The residual represents few percent of the acquired volume but covers a large surface area. In the building direction, the bounding box created at the beginning of each layer is the location of tailed porosities (pore at edge

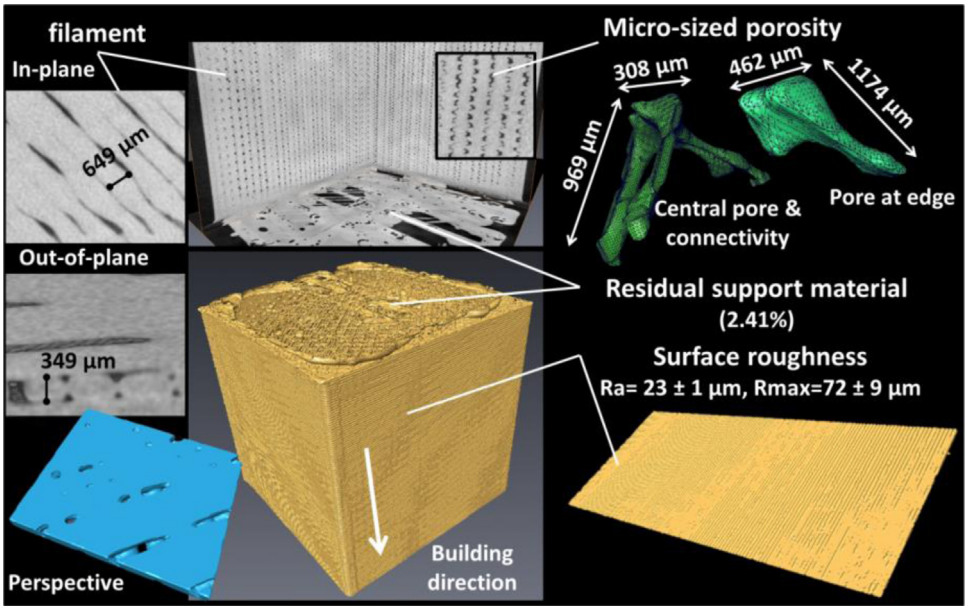

Fig. 2. Characteristic dimensions of microstructural defects induced by 3D printing.

in Fig. 2) form because of the abrupt change in path direction and deceleration of the printing tip. The alternation of filament paths reveals different crossing situations where large connectivity between porosities is likely to appear (central pore in Fig. 2). The mismatch between successive contours (lack of cohesion between successive layers) is the cause of the observed surface topography, which is typical of parts realised using FDM. Both average and maximum roughness values are well below the printing tip size. This is symptomatic of the lack of cohesion between contiguous filaments (out-of-plane view of filament in Fig. 2). The in-plane view of the filament arrangement (left upper sketch in Fig. 2) shows that the lateral filament expansion does not guarantee lateral continuity over two or three typical dimensions (three times the diameter of the printing tip). Discontinuity is then drastically enhanced by the successive layers creating connected porosities along the building direction (central view in Fig. 2). The out-of-plane view of the laying down shows morphological modifications experienced by the filament. The change concerns the circular section which appears as elliptical. The smallest transverse dimension is captured in the building direction, which means that the shape modification is driven by the stretching of the filament combined to the gravitational action of the following layers. The average ratio between the transverse dimensions of the elliptical filament is 326 ± 17 µm for out-of-plane over 586 ± 80 µm for in-plane, which is close to 0.56. Contiguous filaments form also a neck. The limited extension of the neck is the source of the porous morphology highlighted in the same figure. Necking represents the connecting part between filaments. The result of the lack of cohesion, which can be estimated by the extension of the neck, creates the roughness discussed earlier.

Fig. 3 shows perspective views of the porous network in ABS blocks as function of printing orientation. The light grey level represents the porosity arrangement in the printed ABS block. 3D views are illustrated as function of the printing angle (θ). On the left side, perspective views are organised to illustrate the porosity arrangement through the vertical direction (building direction). The images on the right side are top views that illustrate the in-plane arrangement of the porosity network. This porous network reflects the quality of adhesion between contiguous filaments described in Fig. 2.

Indeed, the regular arrangement of porosity follows the path crossing of filament as follows: +45°/−45°, +75°/−15°, +90°/+0°, +15°/−75°, and again +45°/−45° for $\theta = 0°$, 30°, 45°, 60° and 90°, respectively. The change of orientation of the porous network coincides with the angle increment.

Table 1
Porosity statistics from analysis of X-ray µ-tomography of printed ABS samples as function of printing angle.

θ (°)	f (%)	δf_x	δf_y	δf_z	Mxf_x	Mxf_y	Mxf_z	γ_{26} (%)	γ_6 (%)
0	5.07	3.01	2.95	0.97	20.94	18.78	10.39	85.04	79.54
30	4.57	2.21	2.24	1.09	20.13	23.69	9.87	76.60	75.10
45	6.12	7.04	6.33	1.11	45.29	44.84	11.13	62.11	61.84
60	4.51	2.26	2.32	1.00	17.09	18.70	9.41	71.68	69.32
90	4.84	1.97	2.70	1.16	11.68	15.23	9.82	78.33	74.49

The alternation of the layers follows a logic of 45°/−45° for $\theta = 0°$. Layers rotate by 30° about the building direction for each angle increment.

Resolution coarsening effects on both pore content and connectivity are explored in Fig. 4.

Pore content is stable up against resolution lowering down to a coarsening factor of 0.1. This means that scaling each dimension of the original image to its one tenth does not affect the prediction of elasticity constants. These are exclusively dependent on the phase content. Pore connectivity resits resolution lowering down to a coarsening factor of 0.4. Since all computations of structural attributes are conducted at full resolution ($\lambda = 1$), connectivity results are representative of the 3D printing effect.

The examination of the porosity level as function of sample orientation indicates slight differences (standard deviation of 0.66%) between studied configurations (Table 1).

The largest porosity level is obtained for 3D printing configurations with $\theta = 45°$. The results summarised in Table 1 demonstrate that the porosity level is acceptable (<6.2%) for all situations. However, the scatter in porosity levels measured in all space directions ($\delta f_x, \delta f_y, \delta f_z$) indicates a strong anisotropy (Table 1). The largest scatter in porosity level is observed in x- and y-directions. This scatter represents, in the average or irrespective of the orientation, 63%, 64% and 22% of the average porosity level in X-, Y- and Z-directions, respectively. The small fluctuation of porosity measured in the building direction (22%) compared to the remaining directions is an evidence of a higher homogeneity in porosity arrangement through the building direction. The worse

configuration corresponds to θ = 45°, where the porosity fluctuations in x- and y-directions are the largest ones.

Fig. 5 depicts the axial profiles of porosity content in main space directions as function of orientation angle (θ). These profiles depict how the porous network is arranged in particular direction. These

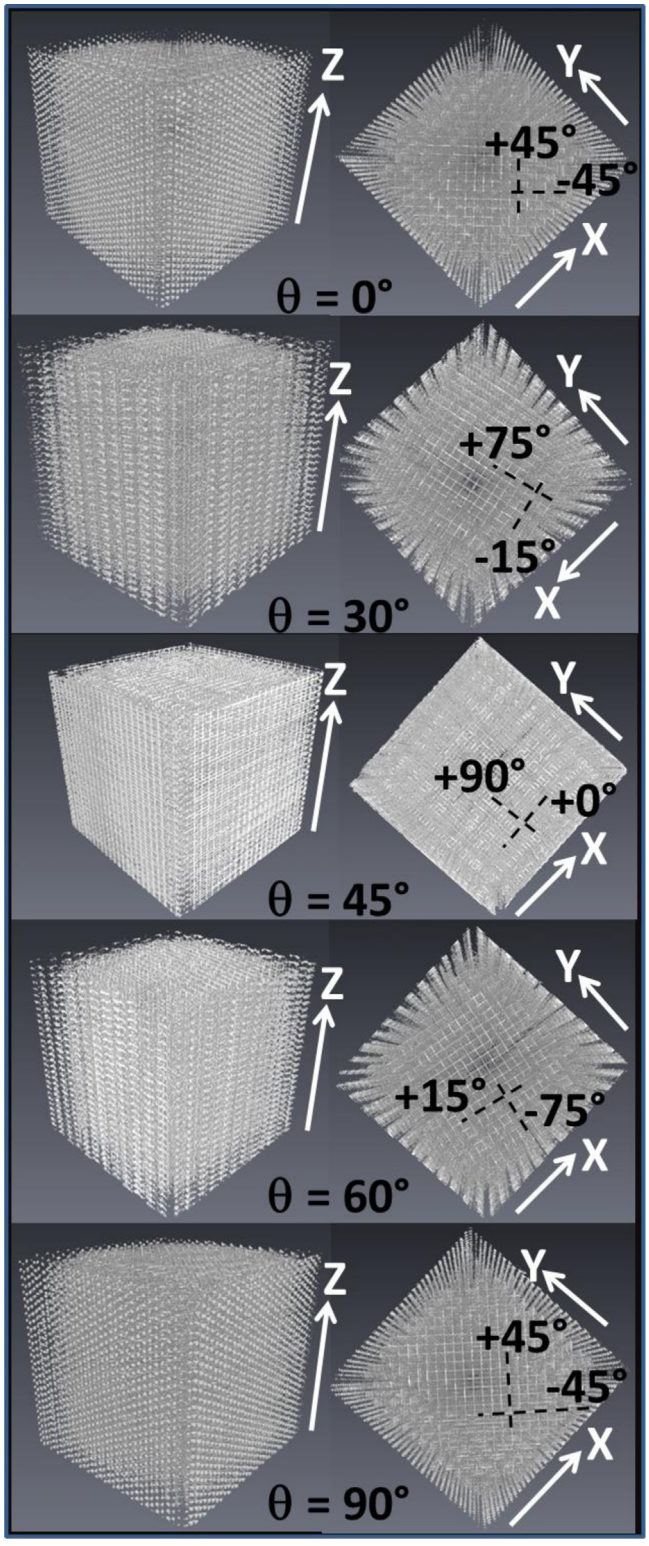

Fig. 3. 3D views showing the porous network as function of printing angle θ. Porosity is labelled with a light grey level.

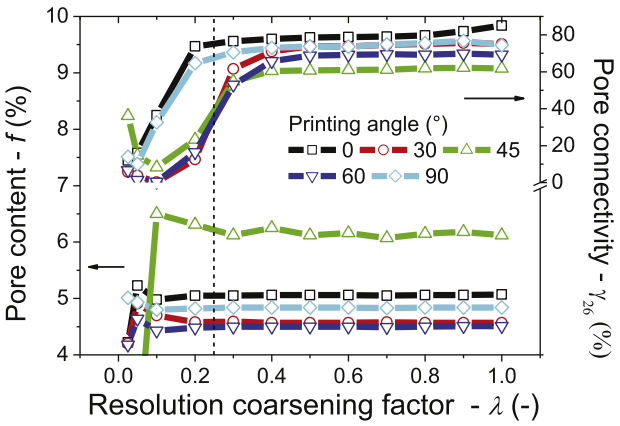

Fig. 4. Effects of resolution coarsening on pore connectivity and content.

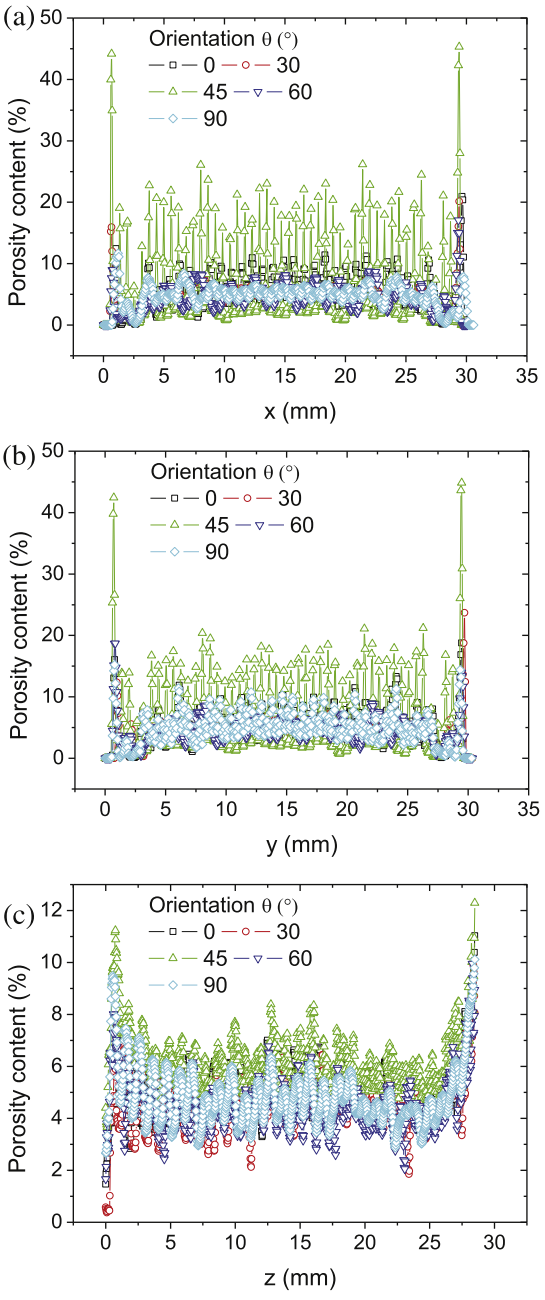

Fig. 5. Axial porosity levels as function of sample orientation angle (θ) in (a) X-, (b) Y- and (c) Z-directions.

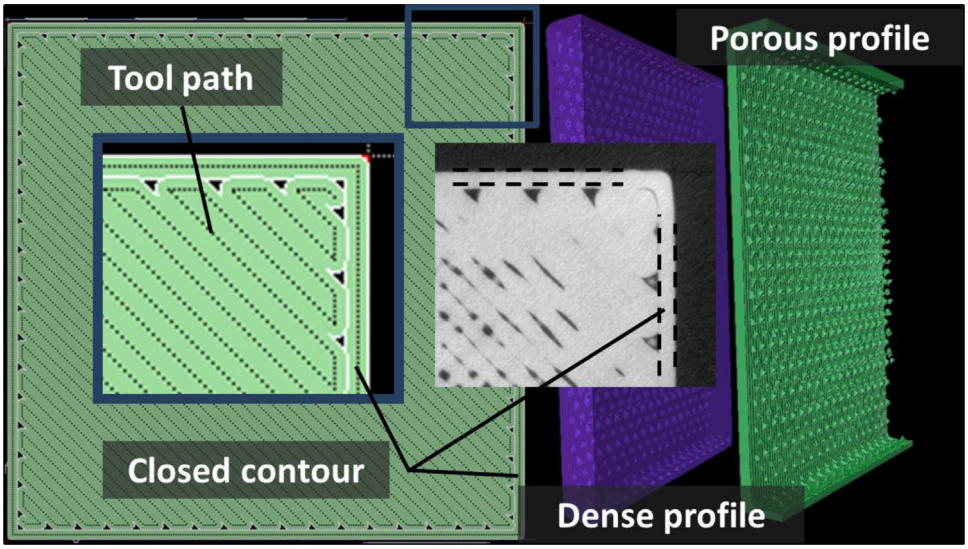

Fig. 6. Tool path generation logic illustrating the close contour in XY plane (perponducilar to the building direction) in comparison with the microstructural rendering at the border of the printed ABS.

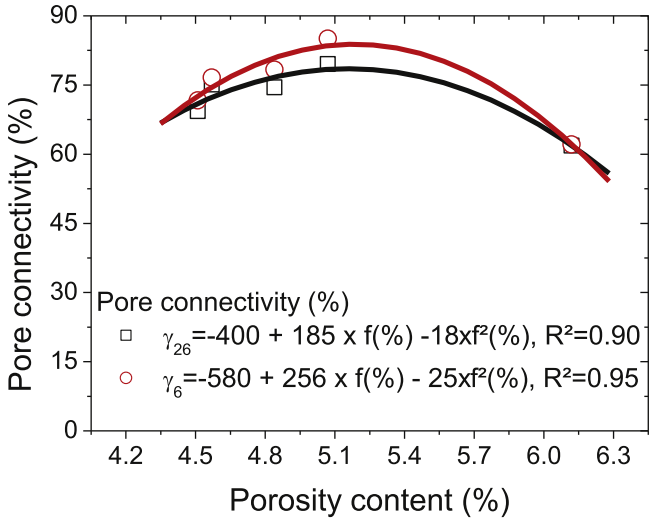

Fig. 7. Relationship between pore connectivity and porosity content.

profiles are thus informative of any anisotropy taking place across the layers of printed ABS.

This information is not accessible through average quantities depicted in Table 1. In addition, axial profiles allow the ranking of such anisotropy because of marked differences between printing angles in different space directions. Fig. 5a shows the porosity content profile in X-direction for all printing angles. A typical U-form illustrates the type of anisotropy exhibited by the axial porosity distribution (Fig. 5a). The axial profile of porosity content in Y-direction looks similar from the heterogeneity viewpoint (Fig. 5b). Both profiles represent in some way the in-plane porosity arrangement, which is different from the out-of-plane profile (Fig. 5c). The difference is related to the fact that porosity content is larger than 3% at most Z positions (Fig. 5c) while porosity content in any in-plane position alternates between the ground value and larger levels (Fig. 5a and b). Despite these differences, all profiles present limited porosity levels at both ends, which are followed by large peaks. The corresponding abscissa positions correspond to the printed part skin or envelope. The absence of porosity at these particular positions indicates the presence of a thin dense band surrounding the printed feature. The genesis of this band is related to the logic behind the toolpath generation (Fig. 6). Indeed, Fig. 6 designates qualitatively the type of geometrical anisotropy associated to the porous network. Within this band (marked with dash lines in Fig. 6), no porosity is detected in a typical thickness varying between 360 μm and 780 μm. The close contour confers to the printed structure mechanical stability to the skin and ensures compactness. This comes at a cost as can be deduced from the microstructural analysis (Fig. 6). Filament path mismatch creates a lack of space filling represented by limited extension of filament necking. Thus, large porosities follow immediately the dense contour, whose effect is reflected by the observed porosity content peaks in Fig. 5. These peaks vary in intensity depending on the printing angle θ. The formed porosity under the skin has a large connectivity and a typical form shown in Fig. 2 (edge porosity).

The porosity peak is associated to the laying down mismatch when the printing tip changes rapidly the path direction towards the next pass. So, the largest porosity levels in axial profiles correspond to the alteration of material deposition at the boundaries. The peak of porosity content can be as large as 45% (Fig. 5a and b) as also shown in Table 1. In X- and Y- directions, similar high fluctuations of porosity profiles are observed (Fig. 5a and b). The lowest fluctuations in porosity are observed in the building direction (Fig. 5c). For all cases, axial fluctuations in porosity are associated to the defects induced by crossed or aligned filaments. Among all studied configurations, θ = 45° achieves the highest levels of porosity fluctuations. Indeed, the corresponding axial profile of porosity content in Fig. 5a presents peaks of about 20% (if excluding the largest peaks associated to the skin). The largest levels do not exceed 10% for the remaining printing angles. A similar comment goes also for the other in-plane axial profiles shown in Fig. 5b. The out-of-plane profiles (Fig. 5c) still show the same ranking but the difference is secondary compared to the in-plane axial profiles. Most of these peaks are below 8% for θ = 45° whereas these are smaller than 6% for the remaining printing angles.

The large fluctuations in porosity profile observed for θ = 45° contrast with the results of pore connectivity summarised in Table 1. Indeed, the former orientation is correlated to the lowest pore connectivity among all possible orientations. The largest pore connectivity is obtained for the angles 0° and 90°. Eq. (7) suggests that pore connectivity results (Table 1) can be due to either a change of the volume of the largest pore, or to a different porosity content which could be due to a higher amount of pores at the

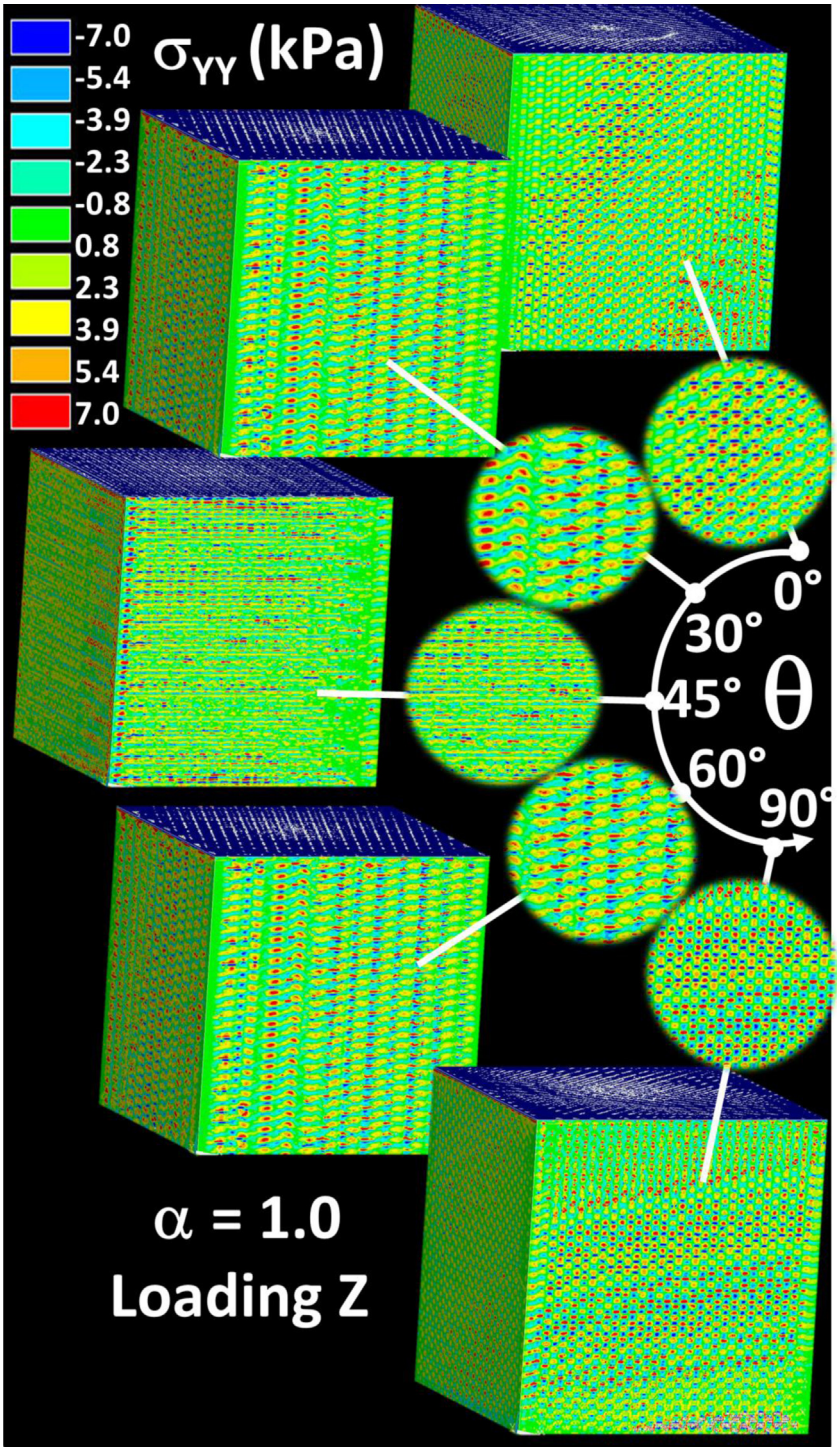

Fig. 8. Stress component σ_{YY} contourplots of at full scale ($\alpha = 1.0$) as function of printing angle θ.

edges. If pore connectivity is only driven by the increase of porosity content, a linear decreasing trend should be obtained. The plot of the pore connectivity as function of porosity content (Fig. 7) shows that this is not true for almost printing angles. The trend is more parabolic even if face connectivity (γ_6) is used. This trend suggests that pore connectivity is more related to the volume variation of the largest connected pore.

The results of face connectivity (γ_6) show that this scheme is responsible for the loss of about 2.69% of pore connectivity as shown in Table 1. This result indicates that this loss is minor and confirms that most of the porosities are connected through voxel faces.

Fig. 8 illustrates the nodal solutions corresponding to stress component σ_{YY} related to full scale ($\alpha = \beta = 1$) loaded in the building direction. The way the porous network affects the stress distribution is, at the same time, qualitative and quantitative information. This information is retrievable through the magnitude and distribution of stress in the contourplots (Figs. 8 and 9). If this information is retrieved as function of printing angle and sampling ratio, the effect of process induced imperfections on elasticity behaviour of printed ABS is captured.

The stress fields reveal heterogeneous distribution affected by the presence of porosities, which act as stress concentrators. The

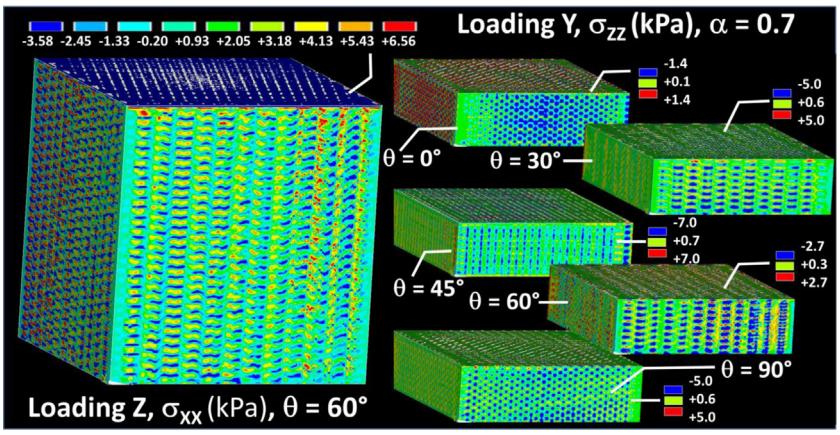

Fig. 9. Effect of vertical sampling on stress component contourplots (on the right σ_{ZZ} for loading in lateral direction −Y and $\alpha = 0.7$) for different printing angles θ. On the left stress component σ_{XX} at full scale ($\theta = 60^\circ$, $\alpha = 1.0$, loading in building direction − Z) is also illustrated.

Table 2
Statistical analysis of elasticity response of 3D printed ABS. Min, AVE, STD are minimum, average and standard deviation operators.

θ(°)	Lateral sampling—β					Vertical sampling—α				
	0	30	45	60	90	0	30	45	60	90
$\mu(EX)$	0.97	0.94	0.96	0.96	0.96	0.99	0.99	0.99	0.99	0.99
$\mu(EY)$	0.96	0.94	0.96	0.96	0.97	0.99	0.99	0.99	0.99	0.99
$\mu(EZ)$	0.98	0.97	0.97	0.98	0.99	0.99	0.99	0.99	0.99	0.99
$\delta(EX)$	1.13	1.88	1.06	1.18	1.21	0.43	0.29	0.36	0.22	0.25
$\delta(EY)$	1.21	1.76	0.93	1.36	1.09	0.43	0.35	0.29	0.28	0.25
$\delta(EZ)$	0.63	0.99	0.66	0.58	0.48	0.49	0.36	0.28	0.27	0.24
$\omega(EX, EY, EZ)$	1.04	1.04	1.03	1.03	1.04	1.02	1.01	1.02	1.01	1.02
$\gamma(EX, EY)$	0.13	0.38	0.23	0.50	0.27	0.05	0.23	0.10	0.36	0.09
$\gamma(\nu_{xy}, \nu_{yx})$	0.13	0.38	0.20	0.50	0.27	0.03	0.24	0.10	0.41	0.09
$\gamma(\nu_{xz}, \nu_{yz})$	0.04	0.14	0.04	0.16	0.02	0.00	0.03	0.04	0.02	0.02
$\gamma(\nu_{zx}, \nu_{zy})$	0.12	0.35	0.21	0.54	0.27	0.03	0.24	0.16	0.48	0.09
$\delta(\nu_{xy})$	0.09	0.75	0.48	0.52	0.20	0.05	0.19	0.19	0.15	0.06
$\delta(\nu_{zy})$	0.51	0.76	0.41	0.63	0.40	0.21	0.29	0.21	0.24	0.18
$\delta(\nu_{yx})$	0.20	0.83	0.64	0.35	0.19	0.05	0.14	0.25	0.10	0.04
$\delta(\nu_{zx})$	0.43	0.88	0.55	0.48	0.52	0.20	0.17	0.29	0.18	0.20
$\delta(\nu_{xz})$	0.16	0.24	0.22	0.22	0.15	0.08	0.07	0.06	0.04	0.04
$\delta(\nu_{yz})$	0.12	0.27	0.25	0.20	0.14	0.09	0.04	0.04	0.05	0.05

revealed distributions show alternation of compressive and tension stresses (Figs. 8 and 9). When subjected to uniaxial loading, compressive stresses develop around pore edges aligned with the loading direction and tensile stresses elsewhere. Crack initiation is likely to occur from the porosity contours under tension as a result of localisation. Since finite element computation is based on meshing of X-ray stacks, the stress distribution highlights thus the signature of porosity morphology and connectivity.

The alternation of compressive and tensile stresses differs significantly depending on the printing orientation but marked differences in terms of magnitude are not observed. Stress localisation is expected to induce significant damage percolation. This is evidenced by the aligned domains of isostress in particular directions.

Fig. 9 shows the predicted stress distributions for a constant vertical sampling along the building direction ($\alpha = 0.7$).

On the right side, stress component σ_{ZZ} is compared for different printing angles for the same vertical sampling ($\alpha = 0.7$). Alternation of compressive and tension stresses are evidenced for all printing angles. The magnitudes of the minimum and maximum stress levels are adapted to show the spatial periodicity of the heterogeneous stress field. The stress heterogeneity is marked by a regular alternation of low and large stress levels, which is a characteristic of the printing process. These levels follow the porous arrangement since the porosity contours are regions of larger stress levels and stress localisation. This confirms the role of local heterogeneities that affect the spatial distribution of stress field. Periodicity of the stress field is correlated to the orientation of the printed block and varies depending on the printing angle. The periodicity of the stress distribution is also preserved through a large range of vertical sampling. On the right side in Fig. 9, stress component σ_{XX} issued for a loading in Z-direction at the full scale ($\alpha = 1$) exhibit similar characteristics with the stress distributions on the right side ($\theta = 30^\circ$ and $\theta = 60^\circ$). The highest heterogeneity is thus obtained equivalently by loading the sample in X or Y directions and issuing the component σ_{ZZ} or by loading the same structure in Z-direction and issuing the components σ_{XX} or σ_{YY}. All stress distributions confirm also that the average intensity does not differ too much from one printing angle to another. This is also expected from the analysis of porosity content in Table 1.

Fig. 10 compares the predicted tendencies for Young's modulus in all space directions as a function of orientation and sampling for an increasing lateral (β) directions. Young's moduli trends are scaled with respect to Young's modulus of the as-received ABS material. An overall trend showing alternation of lower and higher Young's moduli is highlighted. This jagged variation of all investigated Young's moduli components is to be correlated with the spatial periodicity of the defects as attested by the porosity profiles in Fig. 5. However, such alternation appears to be of limited magnitude as attested by the quantity $\mu(-)$

$$\mu(EX) = Min(EX_{\forall s}) / Max(EX_{\forall s}) \quad (14)$$

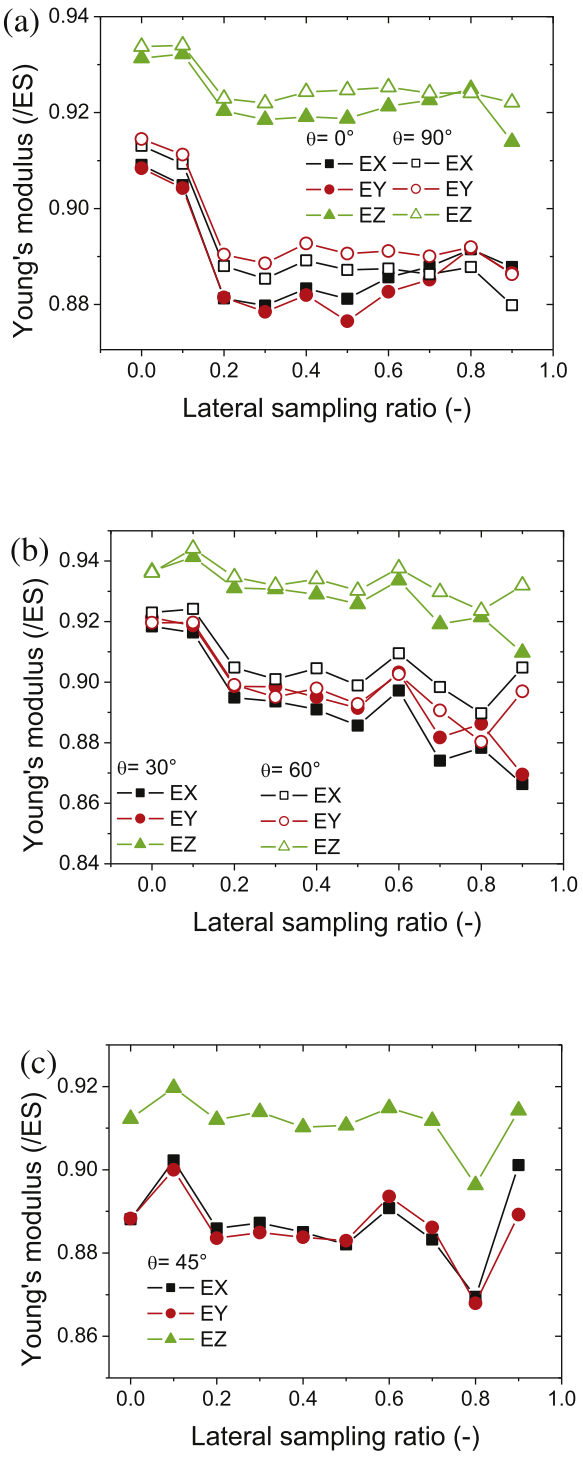

Fig. 10. Effect of lateral sampling ratio (β) on Young's moduli for all printing angles (θ).

where the subscript s refers to any sampling in lateral (β) or vertical (α) directions.

Similar expressions are derived for EY and EZ for both lateral and normal sampling ratios as follows

$$\mu(EY) = Min(EY_{\forall s})/Max(EY_{\forall s}) \quad (15)$$

$$\mu(EZ) = Min(EZ_{\forall s})/Max(EZ_{\forall s}) \quad (16)$$

where the intensities of $\mu(EX)$, $\mu(EY)$ and $\mu(EZ)$ are shown in Table 2.

In Fig. 10, the predicted tendencies show qualitatively similarities between tendencies in X and Y directions, which means that reasonably the relationship ($EX \approx EY$) holds for any orientation and sampling situation.

Qualitative analysis of these results shows a transverse isotropy perceivable for all orientations more particularly for θ = 45° ($\gamma(EX, EY)$ in Table 2). Indeed, Fig. 10c shows that Young's moduli EX and EY have the closest trends. For the remaining curves (Fig. 10a and b), the tendencies exhibited by EZ is distinct for all lateral sampling ratios. The predicted transverse isotropy is quantitatively confirmed from the small scatter (≤0.40%) between EX and EY expressed using the quantity $\gamma(EX, EY)$

$$\gamma(EX, EY) = 100 \times STD(EX_{\forall s}, EY_{\forall s})/AVE(EX_{\forall s}, EY_{\forall s}) \quad (17)$$

The extent of the transverse isotropy is also limited for all studied cases, which is revealed from the quantity

$$\omega(EX, EY, EZ) = AVE(EX_{\forall s}, EY_{\forall s})/EZ_{\forall s} \quad (18)$$

In the full range of sampling, the variation of all engineering constants including Young's moduli is expressed using another quantity δ which writes as follows

$$\delta(\Theta) = 100 \times STD(\Theta_{\forall s})/AVE(\Theta_{\forall s})|\Theta = EX, EY, EZ, \nu_{xy}, \nu_{zy}, \nu_{yx}, \nu_{zx}, \nu_{xz}, \nu_{yz} \quad (19)$$

This quantity seems to be also limited (δ < 2%) for all components EX, EY and EZ irrespective of orientation and type of sampling (Table 2).

Similar responses are shown in Fig. 11 for Poisson's ratios (ν_{yx}, ν_{zx}, ν_{xy}, ν_{zy}, ν_{xz}, and ν_{yz}) resulting from the combination of lateral sampling and orientation.

The examination of all trends confirms minor jagged variations of Poisson's coefficients with respect to lateral sampling ratio like in the former case (Fig. 10). Similarly to the former expression relating in-plane Young's moduli components EX and EY, the predicted transverse isotropy is also quantified using the quantities

$$\gamma(\nu_{xy}, \nu_{yx}) = 100 \times STD(\nu_{xy_{\forall s}}, \nu_{yx_{\forall s}})/AVE(\nu_{xy_{\forall s}}, \nu_{yx_{\forall s}}) \quad (20)$$

$$\gamma(\nu_{xz}, \nu_{yz}) = 100 \times STD(\nu_{xz_{\forall s}}, \nu_{yz_{\forall s}})/AVE(\nu_{xz_{\forall s}}, \nu_{yz_{\forall s}}) \quad (21)$$

And

$$\gamma(\nu_{zx}, \nu_{zy}) = 100 \times STD(\nu_{zx_{\forall s}}, \nu_{zy_{\forall s}})/AVE(\nu_{zx_{\forall s}}, \nu_{zy_{\forall s}}) \quad (22)$$

The trends in Fig. 11 show that the following relationships can be deduced

$$\nu_{xy} \approx \nu_{yx}; \nu_{xz} \approx \nu_{yz}; \nu_{zx} \approx \nu_{zy} \quad (23)$$

The validity of all equalities in Eq. (23) against sample orientation is illustrated in Table 2 by the analysis of the quantities $\gamma(\nu_{xy}, \nu_{yx})$, $\gamma(\nu_{xz}, \nu_{yz})$ and $\gamma(\nu_{zx}, \nu_{zy})$ for both sampling types. These quantities are below 0.60%, confirming the transverse isotropy in all cases irrespective of sampling ratios (α and β).

Intensity of Poisson's coefficients shown in Fig. 11 are of limited variation as confirmed by the quantities $\delta(\nu_{xy})$, $\delta(\nu_{yx})$, $\delta(\nu_{xz})$, $\delta(\nu_{zx})$, $\delta(\nu_{yz})$ and $\delta(\nu_{zy})$.

5. Conclusions

X-ray micro-tomography reveals that fused deposition modelling results in large modification of ABS filament geometry. The in-plane laying down of the fused material is not continuous. Contiguous filaments exhibit evident lack of cohesion running through the millimetre scale. This is a limiting factor against geometry accuracy. The circular cross-section of ABS filament transforms to an elliptical one with shape factor as small as 0.54. The measured

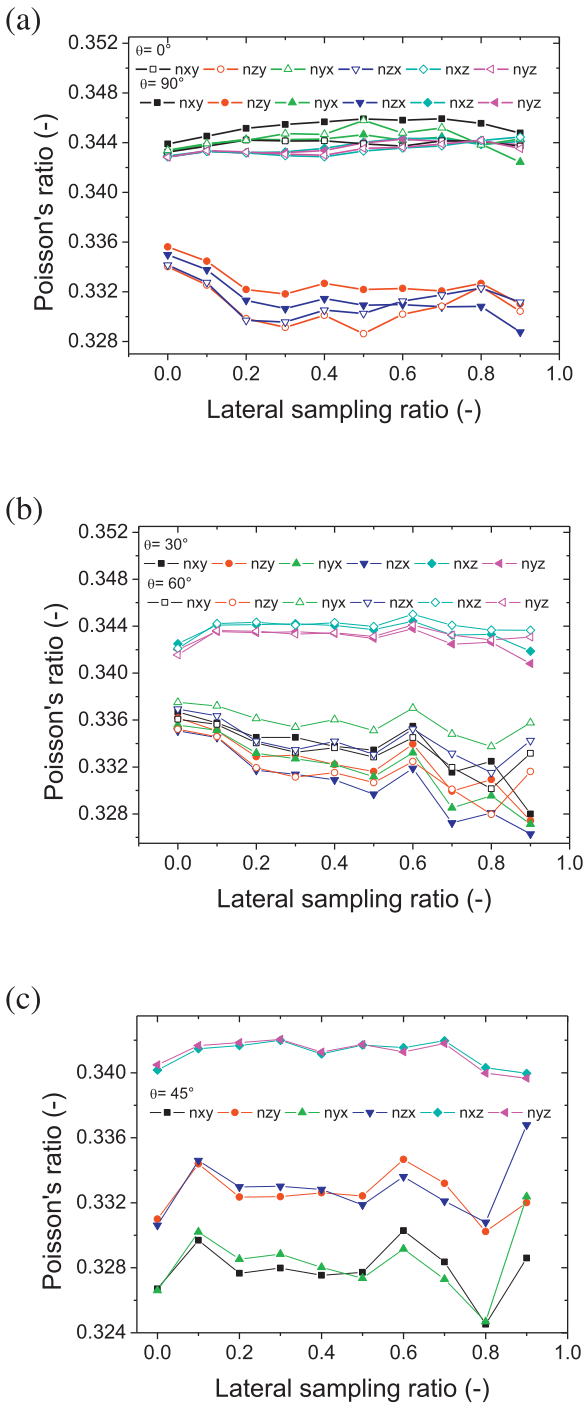

Fig. 11. Effect of lateral sampling (β) on Poisson's ratios for all printing angles (θ).

amount of porosity of less than 6.2% is not limiting for the design rather than pore connectivity which is, in the best case, above 62%. This can be a serious issue for the mechanical performance at rupture point. The relative stability of all computed engineering constants against sampling results from the combination of small porosity content and regularity of its spatial arrangement. This is supported by the similarities of the heterogeneous stress distributions and low scatter of engineering constants (less than 1% for both Young's moduli and Poisson's ratios) predicted for large range of lateral and vertical samplings.

The authors believe that the large connectivity in the porous network and the lack of cohesion between filaments in printed materials need to be related to stress and strain localisation for a better understanding of the anisotropy effects. The CAD model should not be the starting geometry for such analysis but the path generation result is, since interfaces are only known at this stage. The mechanical performance of the printed parts can be more precisely anticipated if adequate interfacial laws are implemented. This will be a first step towards realistic optimisation of parts designed using FDM where optimal path generation is not exclusively decided by space filling requirement but also by smart filament arrangement that guarantees adaptable mechanical stability.

Acknowledgements

The authors would like to thank Pierre Malige and Julien Grison, from IUT of Nantes, for their technical assistance on the 3D printing process and mechanical testing. The authors gratefully acknowledge the International Campus on Safety and Intermodality in Transportation (CISIT), the Nord-Pas-de-Calais Region and the European Community (FEDER funds) for partly funding the X-ray tomography equipment.

References

Ahn, S.H., Montero, M., Odell, D., Roundy, S., Wright, P.K., 2002. Anisotropic material properties of fused deposition modeling ABS. Rapid Prototyp. J. 8, 248–257.
Ayadi, A., Nouri, H., Guessasma, S., Roger, F., 2015. An original approach to assess elastic properties of a short glass fibre reinforced thermoplastic combining X-ray tomography and finite element computation. Compos. Struct. 125, 277–286.
Baker, D.R., Mancini, L., Polacci, M., Higgins, M.D., Gualda, G.A.R., Hill, R.J., Rivers, M.L., 2012. An introduction to the application of X-ray microtomography to the three-dimensional study of igneous rocks. Lithos 148, 262–276.
Becker, R., Grzesiak, A., Henning, A., 2005. Rethink assembly design. Assembly Autom. 25, 262–266.
Carneiro, O.S., Silva, A.F., Gomes, R., 2015. Fused deposition modeling with polypropylene. Mater. Des. 83, 768–776.
Chakraborty, D., Reddy, B.A., Choudhury, A.R., 2008. Extruder path generation for curved layer fused deposition modeling. Comput. Aided Des. 40, 235–243.
Choi, J.W., Medina, F., Kim, C., Espalin, D., Rodriquez, D., Stucker, B., Wicker, R., 2011. Development of a mobile fused deposition modeling system with enhanced manufacturing flexibility. J. Mater. Process. Technol. 211, 424–432.
Galantucci, L.M., Lavecchia, F., Percoco, G., 2008. Study of compression properties of topologically optimized FDM made structured parts. CIRP Ann. Manuf. Technol. 57, 243–246.
Guessasma, S., Babin, P., Della Valle, G., Dendievel, R., 2008. Relating cellular structure of open solid food foams to their Young's modulus: finite element calculation. Int. J. Solids Struct. 45, 2881–2896.
Huang, S.H., Liu, P., Mokasdar, A., Hou, L., 2013. Additive manufacturing and its societal impact: a literature review. Int. J. Adv. Manuf. Technol. 67, 1191–1203.
Kietzmann, J., Pitt, L., Berthon, P., 2015. Disruptions, decisions, and destinations: enter the age of 3-D printing and additive manufacturing. Bus Horiz. 58, 209–215.
Lee, C.S., Kim, S.G., Kim, H.J., Ahn, S.H., 2007. Measurement of anisotropic compressive strength of rapid prototyping parts. J. Mater. Process. Technol. 187, 627–630.
Li, S., Zhao, S., Hou, W., Teng, C., Hao, Y., Li, Y., Yang, R., Misra, R.D.K., 2016. Functionally graded Ti-6Al-4V meshes with high strength and energy absorption. Adv. Eng. Mater. 18, 34–38.
Maire, E., Withers, P.J., 2014. Quantitative X-ray tomography. Int. Mater. Rev. 59, 1–43.
Mamlouk, H., Guessasma, S., 2013. Finite element simulation of the compression behaviour of airy breakfast cereals. Innov Food Sci. Emerg. 19, 190–203.
Mizutani, R., Suzuki, Y., 2012. X-ray microtomography in biology. Micron 43, 104–115.
Mohamed, O.A., Masood, S.H., Bhowmik, J.L., 2015. Optimization of fused deposition modeling process parameters: a review of current research and future prospects. Adv. Manuf. 3, 42–53.
Moreno-Atanasio, R., Williams, R.A., Jia, X., 2010. Combining X-ray microtomography with computer simulation for analysis of granular and porous materials. Particuology 8, 81–99.
Mostefai, N., Hamzaoui, R., Guessasma, S., Aw, A., Nouri, H., 2015. Microstructure and mechanical performance of modified hemp fibre and shiv mortars: discovering the optimal formulation. Mater. Des. 84, 359–371.
National Institute of Health. NIH, MD, USA. http://imagej.nih.gov/ij/.
Nune, K.C., Misra, R.D.K., Gaytan, S.M., Murr, L.E., 2014. Biological response of next-generation of 3D Ti-6Al-4V biomedical devices using additive manufacturing of cellular and functional mesh structures. J. Biomater. Tissue Eng. 4, 755–771.

Nune, K., Kumar, A., Misra, R., Li, S., Hao, Y., Yang, R., 2016a. Osteoblast functions in functionally graded Ti-6Al-4V mesh structures. J. Biomater. Appl. 30 (8), 1182–1204.
Nune, K.C., Kumar, A., Murr, L.E., Misra, R.D.K., 2016b. Interplay between self-assembled structure of bone morphogenetic protein-2 (BMP-2) and osteoblast functions in three-dimensional titanium alloy scaffolds: stimulation of osteogenic activity. J. Biomed. Mater. Res. A 104, 517–532.
Pham, D.T., Gault, R.S., 1998. A comparison of rapid prototyping technologies. Int. J. Mach. Tool Manuf. 38, 1257–1287.
Shaffer, S., Yang, K.J., Vargas, J., Di Prima, M.A., Voit, W., 2014. On reducing anisotropy in 3D printed polymers via ionizing radiation. Polymer 55, 5969–5979.
Thrimurthulu, K., Pandey, P.M., Reddy, N.V., 2004. Optimum part deposition orientation in fused deposition modeling. Int. J. Mach. Tool Manuf. 44, 585–594.
Turner, B.N., Strong, R., Gold, S.A., 2014. A review of melt extrusion additive manufacturing processes: I. Process design and modeling. Rapid Prototyp. J. 20, 192–204.
Yan, X., Gu, P., 1996. A review of rapid prototyping technologies and systems. Comput. Aided Des. 28, 307–318.
Zhai, Y.W., Lados, D.A., Lagoy, J.L., 2014. Additive Manufacturing: Making Imagination the Major Limitation. JOM 66, 808–816.